IEEE Access
Multidisciplinary | Rapid Review | Open Access Journal

Received 27 May 2023, accepted 12 June 2023, date of publication 20 June 2023, date of current version 28 June 2023.

Digital Object Identifier 10.1109/ACCESS.2023.3288006

RESEARCH ARTICLE

Improving Power Delivery of Grid-Connected Induction Machine Based Wind Generators Under Dynamic Conditions Using Feedforward Linear Neural Networks

SHYAMAL SHIVNEEL CHAND[1], (Student Member, IEEE), RAVNEEL PRASAD[1], HIYE K. MUDALIAR[1], DHIRENDRAN MUNITH KUMAR[1], (Graduate Student Member, IEEE), ADRIANO FAGIOLINI[2], (Member, IEEE), MARCO DI BENEDETTO[3], (Member, IEEE), AND MAURIZIO CIRRINCIONE[1,4], (Senior Member, IEEE)

[1]School of Information Technology, Engineering, Mathematics and Physics, The University of the South Pacific, Suva, Fiji
[2]Mobile & Distributed Robots@Panormous Laboratory (MIRPALab), Department of Engineering, University of Palermo, 90133 Palermo, Italy
[3]Department of Industrial, Electronic and Mechanical Engineering, Roma Tre University, 00154 Rome, Italy
[4]Institute FEMTO-ST, CNRS, 90000 Belfort, France

Corresponding author: Adriano Fagiolini (adriano.fagiolini@unipa.it)

ABSTRACT In the conventional grid-connected Wind Energy Conversion System (WECS), the generator side inverter is typically controlled via Field Oriented Control (FOC), while Voltage Oriented Control (VOC) controls the grid side inverter. However, robust operation cannot be guaranteed during sudden changes in wind speeds and weak grid connections. This paper presents a novel method to improve the overall dynamic performance of on-grid induction machine-based wind generators. An online mechanical parameter estimation technique is devised using Recursive Least Squares (RLS) to compute the machine inertia and friction coefficient iteratively. An adaptive feedforward neural (AFN) controller is also proposed in the synchronous reference frame, which is constructed using the estimated parameters and the system's inverse. The output of the neural controller is added to the output of the speed PI controller in the outer loop of the FOC to enhance the speed response of the wind generator. A similar approach is taken to improve the classical VOC structure for the grid-side inverter. In this case, the RLS estimates the equivalent Thevenin's grid impedance in real-time. As for the adaptive action, two identical neural networks are integrated with the inner loop direct and quadrature axis current PI controllers. Under nominal operating conditions, it is observed that the PI+AFN provides a faster settling time for the generator's speed and torque response. Upon being subjected to variations in the wind speed, the PI+AFN outperforms the classical PI controller and attains a lower integral-time error. In addition, the proposed PI+AFN controller has a better ability to maintain the grid-side inverter stability during stochastic variations in grid impedance. One significant advantage of the proposed control approach is that no data for training or validation is required since the neural network weights are directly the output of the RLS estimator. Hardware verification for the improved FOC for wind generators using the adaptive controller is also made using the DSPACE 1007 AUTOBOX platform.

INDEX TERMS Wind energy conversion, induction generator, grid-connected wind turbine, machine inertia, friction coefficient, grid impedance, feedforward controller, adaptive neural networks, recursive least squares estimator.

I. INTRODUCTION

The focus of the power and energy sector worldwide is transitioning from fossil fuel-based generation to renewable power. Significant investments in solar, hydro and hydrogen

The associate editor coordinating the review of this manuscript and approving it for publication was Zheng Chen.

fuel cells are being made because of promising sustainability and low environmental impacts. Wind Energy Conversion Systems (WECS) is also attracting global attention in industry and research due to advancements in power conversion topologies and profitable manufacturing techniques of wind turbines. However, due to the stochastic nature of wind resources, engineers often encounter difficulties in effectively integrating it with the electricity grid. The power-producing capacity of wind turbines has dramatically increased over the past few decades to multi-megawatt levels. As such, robust and advanced control solutions have to be developed to guarantee power converters' stability during mass integration of power into the network from WECS [1].

Wind Turbine Generators (WTG) can operate at fixed or variable speeds. The Squirrel Cage Induction Generators (SCIG) has the capability of operating in both fixed speed and variable speed mode, while the Doubly-Fed Induction Generators (DFIG) and Permanent Magnet Synchronous Generators (PMSG) usually are operated at variable speeds [1], [2]. Generally, the back-to-back converter topology shown in Figure 1 is widely used for grid-connected WTGs as it provides complete controllability. The three main control subsystems for SCIG include aerodynamic torque control, energy capture maximization and grid active and reactive power regulation. Field Oriented Control (FOC) or Direct Torque Control (DTC) are the most commonly used strategies for the machine side converter (MSC), while Voltage Oriented Control (VOC) is employed for the grid side converter (GSC) [3], [4], [5].

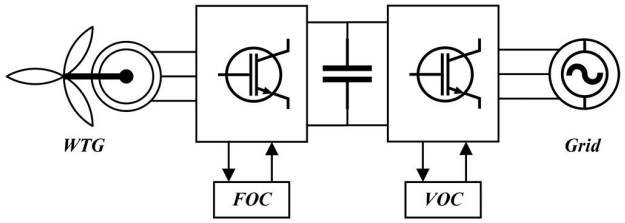

FIGURE 1. Back-to-back converter configuration for WECS.

For the control of the SCIG, FOC primarily uses classical Proportional-Integral (PI) controllers to achieve the desired speed and torque response. However, SCIGs are a typical nonlinear multi-variable robust coupling system whose performance is generally affected by uncertainties such as rapid changes in wind speed and unpredictable parameter variations. As a result, the conventional PI controller encounters difficulties in meeting high-performance requirements [6].

Moreover, to capture maximum power from WTGs, a variable adaptive fuzzy PI control based on stator flux-oriented vector control can be implemented to govern the stator's active and reactive power [7], [8]. For variable-speed wind generators, a nonlinear Integral Backstepping Strategy (IBS) combined with adaptive power control can also assist in optimizing power extraction. The IBS-based tip speed ratio power control method provides improved efficiency and rapid system response compared to the conventional PI approach [9]. Similarly, [10] presents an adaptive backstepping nonlinear control method for variable-speed wind turbines with a PMSG for ensuring maximum power extraction. Using a Lyapunov function, this approach also ensures robustness against uncertainties in stator resistance and rotor flux linkage. Nevertheless, these methods fail to account for variations in the mechanical parameters, such as the generator's inertia and friction coefficient, which can affect the speed response and torque ripples.

The speed control characteristics strongly depend on the appropriate selection of the speed control gains. Therefore, it is necessary to know the varying inertia of the whole system so that the speed controller gains can be adapted [11]. Self-tuned PI controllers are also widely used for grid-interfaced wind turbine systems. Improved Multiband-Structured Subband Adaptive Filter (IMSAF) algorithm can update multiple PI controller gains in the cascaded control loop for the Voltage Source Inverters (VSI). Other optimization algorithms, such as water cycle and genetic algorithms, can substitute the IMSAF depending on the available computational power [12].

On the other hand, for the control of the grid side inverter, linear current controllers such as deadbeat, repetitive, proportional resonant, proportional integral, model predictive and sliding mode controllers are often implemented in the synchronous rotating reference frame [13]. These control approaches can maintain fixed switching frequency and have a relatively simple implementation, but the modulator is sluggish, resulting in a slow transient and dynamic response. The deadbeat and proportional resonant controllers also have a smaller transient region and low Total Harmonic Distortion (THD) in the currents at the Point of Common Coupling (PCC). However, they are not compliant with parameter deviations, noise variation, or model uncertainties [14]. These control techniques also require minimal sampling time and higher inverter switching frequency, which tends to cause loss of power.

There are inconsistencies in PCC impedance caused due to the increasing infiltration of renewable energy into the electricity network. This variation significantly influences the voltage and current of the power converter, as in most cases, a static grid impedance is hardcoded in the control structure. Power injection from RES often faces stability challenges induced by the Thevenin equivalent grid impedance seen by the inverters. To govern the active and reactive power more effectively, [15] and [16] proposed a method to continuously approximate the grid impedance ratio by injecting harmonic currents and computing the Discrete Fourier Transform (DFT) of the voltage response at grid frequency. Similarly, a single frequency voltage can be injected with the inverter voltage at PCC, and the sliding DFT of the corresponding grid voltage and currents can be obtained. An adaptive grid observer can permit real-time grid inductance and resistance estimation [17]. However, the injection of harmonics and additional signals with the inverter currents

deteriorates the grid voltage and current quality at PCC, causing power quality issues and inaccuracies in estimating grid impedances.

Recently, significant advancements have been made in Approximate Dynamic Programming (ADP) algorithms that use incremental optimization procedures to control power converters. Optimal vector control has been developed in [18] using a Recurrent Artificial Neural Network (ANN) trained using Levenberg-Marquardt plus forward accumulation through time algorithm and applied to a single-phase inverter with an LCL filter. Correspondingly, [14] presented a control method based on Model Predictive Control (MPC) with a feedforward ANN to reduce THD and alleviate the steady-state and dynamic performance during loading for the two-level inverter. The decoupling circuit's direct and quadrature control voltages can also be generated through a trained neural network replacing the current controllers [19]. Nevertheless, a substantial drawback of these control algorithms is the appropriate training of the ANN, which needs to be carried out before implementation because the network's weights are determined offline. The ANN's reliability and performance accuracy depends on the type and amount of data used in the training process. Insufficient training can affect the overall system stability and response to changing operating conditions. The use of ANN also increases the computational requirements of processors or control boards during hardware realization.

Thus, a more reliable and robust control technique for back-to-back converter topology for SCIG that accounts for changes in operating conditions is necessary for interfacing wind turbines with the network. This paper proposed an adaptive control theory to enhance the performance of the speed PI controller in the FOC and current PI controllers in the VOC via a feedforward ADALINE neural network. The weights of these networks are dependent on induction generator mechanical parameters (inertia and friction coefficient) and grid impedance which are estimated online using the Recursive Least Squares (RLS) algorithm. This eliminates the necessity for any prior training and validation and testing. The proposed control approach is thoroughly verified under various dynamic conditions such abrupt changes in wind speed and grid impedance deviation. The PI+AFN controller is implemented in the synchronous rotating reference frame and provides better reference tracking capability, minimized overshoots and lower steady state error of the speed, torque and direct/quadrature axis grid currents. The scheme is also verified experimentally on a suitably developed wind turbine emulator using induction machines.

II. MECHANICAL SYSTEM DESCRIPTION

The mechanical subsystem is responsible for extracting the kinetic energy from the wind through turbines and avails it on the rotating shaft of the turbine. In general, the mechanical system is composed of the turbine, gearbox, and the generator connected via high speed and low speed rotor as shown in Figure 2. The low-speed rotor consists of blades that capture the kinetic energy of the wind and convert it into rotational motion. The gearbox is used to increase the rotational speed of the rotor to match the speed required by the generator. The generator is responsible for converting the rotational motion of the rotor into electrical energy. This mechanical power conversion system of a wind turbine can employ various combinations to convert the kinetic energy of wind into electrical energy such as direct drive systems, which eliminate the need for a gearbox, have been gaining popularity due to their simplicity and high reliability. However, they require a larger and heavier generator to handle the rotor's higher torque and lower rotational speed. On the other hand, gearbox drives, which use a gearbox to match the speed required by the generator, can be more efficient for larger turbines, but they can introduce additional mechanical components and potential points of failure. Hybrid drives, which combine elements of direct drive and gearbox drive systems, offer a balance between the efficiency of a gearbox drive and the simplicity of a direct drive. A hybrid drive may use a gearbox to increase the rotational speed of the rotor and then connect directly to the generator. Finally, belt drive systems can use a belt or other flexible coupling to connect the rotor to the generator, reducing the impact of vibration and misalignment on the system. However, belt drives may introduce additional losses and require more frequent maintenance. Therefore, the selection of a mechanical power conversion system for a wind turbine depends on several factors, including the size of the turbine, the wind conditions, and the desired level of reliability and efficiency.

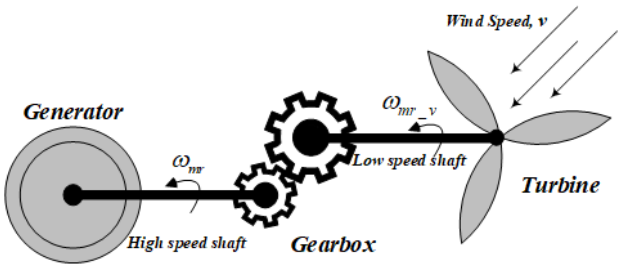

FIGURE 2. Mechanical power conversion system.

The rotation of the low-speed shaft is driven by the energy harvested using the turbines which depends on the speed of the wind. The shaft is connected to a gearbox which enables it to multiply the rotational speed by a suitable ratio across the high-speed shaft connected to the generator. The power captured by the turbine blade is expressed as

$$P_m = C_p(\lambda, \beta)\frac{\rho A}{2}v^3 \tag{1}$$

where P_m is the mechanical power of the turbine, C_p is performance coefficient, A is the area swept by the turbine, ρ is the air density, v is the wind velocity, $\beta$is blade pitch angle, and λ is the Tip Speed Ratio (TSR). TSR is a measure of how fast the tips of the blades of a wind turbine are moving compared to the wind speed. It is calculated by dividing the speed of

the tip of the blade by the speed of the wind. C_p of a wind turbine is a measure of how efficiently the turbine converts the kinetic energy of the wind into mechanical energy. It is defined as the ratio of the power generated by the turbine to the power that would be extracted from the wind if the turbine were 100% efficient. The performance coefficient and the tip speed ratio are expressed as

$$\lambda = \frac{\omega_T R}{v} \tag{2}$$

$$C_p = C_1 \left(\frac{C_2}{\lambda} - C_3\beta - C_4 \right) e^{\frac{-C_5}{\lambda}} + C_5\lambda \tag{3}$$

R is the radius of the turbine, and in equation 3, the $C_1 = 0.5$, $C_2 = 116.0$, $C_3 = 0.4$, $C_4 = 5.0$ and $C_5 = 21.0$. There is a relationship between the TSR and the performance coefficient of a wind turbine. In general, as the TSR increases, the performance coefficient of the turbine also increases. However, the relationship is not linear, and there is an optimal TSR at which the performance coefficient is maximized. This optimal TSR depends on the turbine's specific design and the wind's properties. It is worth noting that the performance coefficient is not the only factor that determines the overall efficiency of a wind turbine. Factors such as the generator's efficiency, bearing losses, and transmission losses also play a role in determining the turbine's overall efficiency [20], [21]. The relationship between the selected turbine TSR and C_p is plotted in Figure 3.

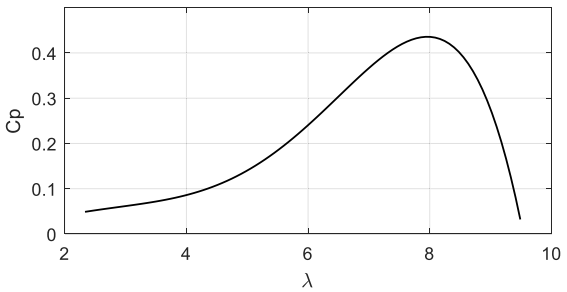

FIGURE 3. Relationship between the tip speed ratio and performance coefficient.

The relation between the mechanical power concerning the rotational speed and the outline parameters is as per Figure 4. The torque produced by the wind turbine is given as

$$T_T = \frac{P_m}{\omega_T} = C_T \frac{\rho \pi R^3}{2} v^2 \tag{4}$$

The graph of mechanical power (P_m) vs. angular velocity (ω_m) for a wind turbine is essential while analyzing the performance of the turbine. This graph displays the relationship between P_m and ω_m, which is commonly referred to as the power curve of the turbine. It demonstrates the amount of power that the turbine can produce at different wind speeds. As the wind speed increases, the power output of the turbine also increases, up to a certain point called the rated power of the turbine. This rated power represents the maximum power output that the turbine is designed to produce.

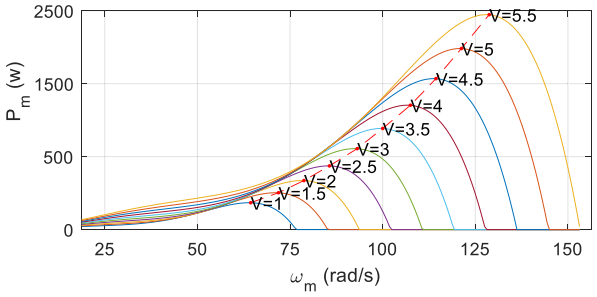

FIGURE 4. Correlation between angular velocity and mechanical power output at different rotor speeds.

The power curve typically has a characteristic shape, which includes a low power output at low wind speeds, a rapid increase in power output as the wind speed increases, and a plateau at the rated power. Beyond the rated power, the turbine's power output begins to decrease, as the turbine is not designed to operate at higher wind speeds. The induction generator and turbine parameters are stated in Table 1.

TABLE 1. Wind generator parameters.

Parameter	Symbol	Value	Unit
Rated power	P_m	2.2	kW
Rated speed	ω_r	157	rad/s
Stator inductance	L_s	0.22	H
Stator resistance	R_s	2.9	Ω
Rotor inductance	L_s	0.23	H
Rotor resistance	R_r	1.52	Ω
Inertia	J_m	$4.8\text{x}10^{-3}$	kg.m^2
Friction Coefficient	B_m	$0.5\text{x}10^{-3}$	N.ms
Air density	ρ	1.20	kg/m^3
Radius	R	2.5	m
Number of poles	N_p	4	-
Gear ratio	n	1:10	-
Tip speed ratio	λ	7	-
Performance coefficient	$C_{p\max}$	0.45	-

An induction generator has been deployed at the wind energy side with the Field Oriented Control (FOC) technique being adopted for the control of the machine. The implemented FOC consists of a double cascaded PI loop, the direct axis also known as the flux loop controls the direct axis current and on the quadrature axis, the speed loop controls the quadrature axis current. In addition, all controllers employ traditional Proportional Integral controllers. Space Vector Modulation (SVM) with a switching frequency of 15kHz has been employed to control the switching of the respective inverters. The use of such a control scheme permits the machine to follow the speed references supplied by any MPPT method with high performance. Since the torque produced by the wind turbine is highly dependent on the

wind speed, a high-performance control technique is always adopted to control the IG. The grid-side inverter provides the DC link voltage control.

On the direct axis, a flux control loop commands the current loop, and a voltage control loop can also command the flux loop to permit the drive to work automatically in the field weakening region by maintaining constant the product of the rotor-flux amplitude and the absolute value of the rotor speed [22]. The voltage reference is compared with the actual voltage, computed as the product of the estimated value of the rotor flux amplitude and the absolute value of the measured rotor speed. An integrator processes the tracking error, and the output of the integrator is the rotor reference flux (ψ_{ref}). The machine's flux is directly proportional to the torque capability of the generator [23].

III. ELECTRICAL SYSTEM DESCRIPTION

The electrical system converts mechanical energy into electrical energy suitable for the grid. It mainly consists of AC-DC and DC-AC inverters, filters, transformers, transmission lines and the grid. The power conversion components and other electrical parameters used in the model are stated in Table 2.

TABLE 2. Electrical parameters.

Parameter	Symbol	Value	Unit
DC Link Capacitor	C_{dc}	1000	µF
Rated DC Voltage	V_{dc}	750	V
Filter Inductance	L_f	25	mH
Filter Resistance	R_f	0.25	Ω
Grid Inductance	L_g	1	mH
Grid Resistance	R_g	0.25	Ω
Switching Frequency	F_{sw}	15	kHz
Utility Voltage	E_{LL}	415	V
Grid Frequency	F_g	50	Hz

The Voltage Oriented Control (VOC) technique regulates the grid-side converter. This technique instantaneously decouples the direct and quadrature components of the injected current concerning the grid voltage vector reference frame. Cross-coupling terms are added to the inverter control voltages in the inner loop to regulate the active and reactive powers at PCC independently. The inverter control voltages for the two axes are generated using equation 5.

$$\begin{aligned} v_{dref} &= \left(K_p + \frac{K_i}{s}\right)\left(i_{dref} - i_{gd}\right) + \omega_g L i_{gq} + v_{gd} \\ v_{qref} &= \left(K_p + \frac{K_i}{s}\right)\left(i_{qref} - i_{gq}\right) - \omega_g L i_{gd} + v_{gq} \end{aligned} \tag{5}$$

i_{dref}/i_{qref} and i_{gd}/i_{gq} are reference and measured direct and quadrature currents, respectively. V_{gd} and V_{gq} are the grid voltages in the synchronous reference frame and ω_g is the angular grid frequency [24]. Consequently, the real and imaginary powers on the AC side in the dq reference frame can be evaluated using

$$\begin{aligned} P &= \frac{3}{2}(v_{gd} i_d + v_{gq} i_q) \\ Q &= \frac{3}{2}(v_{gq} i_d - v_{gd} i_q) \end{aligned} \tag{6}$$

A PI controller in the outer loop generates the reference direct axis current via regulating the DC link voltage. Two PI controllers are also employed in the inner loop to control the direct and quadrature currents injected into the grid. Using the combined output of the current PI controllers and the decoupling circuit, Sinusoidal Pulse Width Modulation (SPWM) technique is employed to generate gate pulses for the IGBT switches. The interconnecting filter is a simple inductor with parasitic resistor in series. Initial grid impedance is kept low to minimize AC voltage harmonics and distortions. The reactive power reference (Q_{ref}) is zero under all test conditions.

IV. PROPOSED ADAPTIVE CONTROL TECHNIQUE

A. ADAPTIVE FIELD ORIENTED CONTROL (AFOC)

When a system, such as the induction generator, is under operation and required to track a rapid reference frame, it requires high bandwidth, making the system less robust and more noise sensitive. As identified earlier, the mechanical parameter of the IG is very sensitive and continuously changes when the machine is in operation. In such cases, to achieve a better performance in reference tracking while keeping noise rejection capacity, one idea is to use a feedforward controller to enhance the required tracking capability of the speed PI controller while leaving the feedback action to stabilize the system and suppress higher frequency disturbance. The scheme proposed and depicted in Figure 5 can be used to increase the reference tracking accuracy and simultaneously be adaptive to the variations of the system parameters. Considering the equation of motion for an electro-mechanical drive,

$$J_m \frac{d\omega}{dt} + B_m \omega_{mr} = \tau_{el} - \tau_L = \Delta\tau \tag{7}$$

where τ_{el} is electromagnetic torque, τ_L is load torque, J_m is inertia, B_m is the viscous friction coefficient, $\Delta\tau$ is the change in torque and ω_{mr} is the measured output speed. Using Euler's discretization with T_s as the sample time, the involved time derivatives is replaced with equation (8)

$$\frac{d\omega_{mr}}{dt} = \frac{\omega_{mr}(k) - \omega_{mr}(k-1)}{T_s} \tag{8}$$

This leads to the following differential equation:

$$\Delta\tau = J_m \frac{\omega_{mr}(k) - \omega_{mr}(k-1)}{T_s} + B_m \omega_{mr}(k-1) \tag{9}$$

Solving equation (9) and expressing it in the form to attain the desired speed ($\omega_{mr}(k)$) yields

$$\omega_{mr}(k) = \left(\frac{J_m - T_s B_m}{J_m}\right)\omega_{mr}(k-1) + \frac{T_s}{J_m}\Delta\tau(k-1) \tag{10}$$

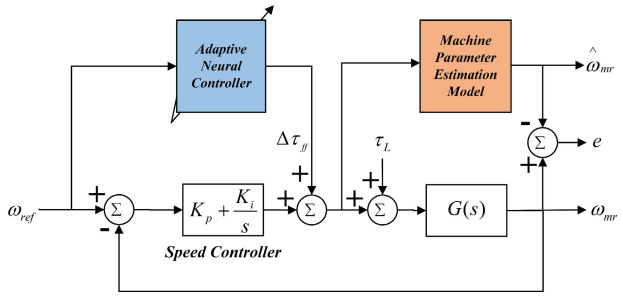

FIGURE 5. General control structure of neural network-based adaptive speed controller.

Defining the coefficients,

$$\alpha_1 = \frac{J_m - T_s B_m}{J_m} \text{ and } \alpha_2 = \frac{T_s}{J_m} \tag{11}$$

Equation (10) can be rewritten as

$$\omega_{mr}(k) = \alpha_1 \omega_{mr}(k-1) + \alpha_2 \Delta\tau(k-1) \tag{12}$$

Given a time window of length N, a linear regressor in the form $Ax \approx b$ can be obtained from equation (12) as

$$\begin{bmatrix} \omega_{mr}(k-1) & \Delta\tau(k-1) \\ \omega_{mr}(k-2) & \Delta\tau k-2) \\ . & . \\ . & . \\ \omega_{mr}(k-N) & \Delta\tau(k-N) \end{bmatrix} \begin{bmatrix} \alpha_1 \\ \alpha_2 \end{bmatrix} \approx \begin{bmatrix} \hat{\omega}_{mr}(k) \\ . \\ . \\ . \\ \hat{\omega}_{mr}(k-N) \end{bmatrix} \tag{13}$$

with b being the actual (measured) speed, x the unknown regressor value to be estimated and A the vector of measure speed over the N sample time window. The full parameter estimation model is shown in Figure 6.

Given this information, a Recursive Least Square (RLS) based estimator is employed to calculate the unknown values for α_1 and α_2. Once α_1 and α_2 are known, equations (11) can then be rearranged, and the varying values for J_m and B_m can be estimated in time using

$$J_m = \frac{T_s}{\alpha_2} \text{ and } B_m = \frac{1-\alpha_1}{\alpha_2} \tag{14}$$

Once the machine is under operation and experiences a change in J_m and/or B_m, the weights can be calculated and be used to construct the inverse of the system. The feedforward controller is created by multiplying the system for the corresponding reference value,

$$\Delta\tau_{ff} = \frac{1}{\alpha_2}\omega_{mr}(k) - \frac{\alpha_1}{\alpha_2}\omega_{mr}(k-1) \tag{15}$$

Equation (15) is an ADALINE neural network with α_1 and α_2 as its weights. When the output of the linear neural network (computed feedforward torque) is added in the speed loop, it will aid the PI controller in improving the machine's performance under dynamic conditions such as abrupt wind speed variation and changes in system inertia and/or friction coefficient. The controller parameters for the adaptive FOC are stated in Table 3.

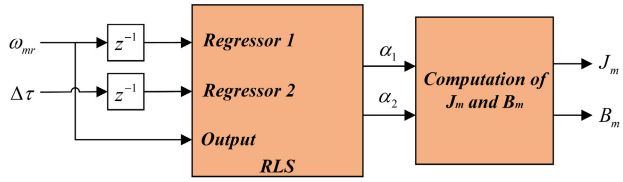

FIGURE 6. Estimation model for generator inertia and friction coefficient.

TABLE 3. Adaptive FOC parameters.

	K_p	K_i
Speed Controller	0.45	3.5
Torque Controller	20	0.6
Flux Controller	100	6
Direct Axis Current Controller	330	2359
Quadrature Axis Current Controller	330	2359
Controller Sample Time (T_s)	100µs	
Covariance Matrix	[1x10^{-4} 1x10^{-4}]	
Forgetting Factor	1	

B. ADAPTIVE VOLTAGE ORIENTED CONTROL (AVOC)

A similar control approach to the one presented in section IV-A can be adopted to enhance the grid-side inverter's stability under varying grid impedance and changing injected currents from the wind turbine. In the scenario of an inverter connected to the grid, the equivalent Thevenin's impedance, as seen at the PCC, can be identified as follows. Primarily, the interconnection between the voltage of the inverter ($v_{\alpha\beta}$) and the grid ($e_{\alpha\beta}$) in the stationary reference frame can be portrayed as in Figure 7.

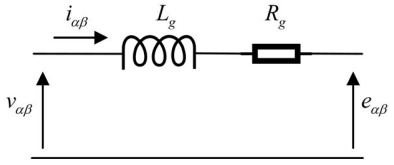

FIGURE 7. Inverter and grid voltage at the equivalent Thevenin's impedance.

Then the inverter voltages can be obtained by taking Clarke's transformation of the three-phase voltages at PCC. As such, $v_{\alpha\beta}$ and $e_{\alpha\beta}$ can be expressed as

$$\begin{aligned} v_{\alpha\beta} &= v_\alpha + jv_\beta \\ e_{\alpha\beta} &= e_\alpha + je_\beta \end{aligned} \tag{16}$$

Considering the input current from the inverter side as $i_{\alpha\beta}$, the voltage drop on the grid impedance can be expressed as

$$v_{\alpha\beta} - e_{\alpha\beta} = L_g \frac{di_{\alpha\beta}}{dt} + R_g i_{\alpha\beta} \tag{17}$$

Denoting the voltage drop at the impedance as

$$u_{\alpha\beta}(k) = v_{\alpha\beta}(k) - e_{\alpha\beta}(k) \tag{18}$$

With T_s as the sample time, using the forward difference Euler's discretization, equation (17) in discrete form becomes,

$$u_{\alpha\beta}(k-1) = L_g \frac{i_{\alpha\beta}(k) - i_{\alpha\beta}(k-1)}{T_s} + R_g i_{\alpha\beta}(k-1) \tag{19}$$

Solving equation (19) for the desired current response$i_{\alpha\beta}(k)$ at an instance of time k yields

$$i_{\alpha\beta}(k) = \frac{L_g - T_s R_g}{L_g} i_{\alpha\beta}(k-1) + \frac{T_s}{L_g} u_{\alpha\beta}(k-1) \tag{20}$$

Assuming,

$$\beta_1 = \frac{L_g - T_s R_g}{L_g} and \beta_2 = \frac{T_s}{L_g} \tag{21}$$

Equation (20) can be rewritten as

$$i_{\alpha\beta}(k) = \beta_1 i_{\alpha\beta}(k-1) + \beta_2 u_{\alpha\beta}(k-1) \tag{22}$$

This allows the formation of an expression in the form of $Ax \approx b$ based on a moving time window of N samples.

$$\begin{bmatrix} i_{\alpha\beta}(k-1) & u_{\alpha\beta}(k-1) \\ i_{\alpha\beta}(k-2) & u_{\alpha\beta}(k-2) \\ . & . \\ . & . \\ i_{\alpha\beta}(k-N) & u_{\alpha\beta}(k-N) \end{bmatrix} \begin{bmatrix} \beta_1 \\ \beta_2 \end{bmatrix} \approx \begin{bmatrix} i_{\alpha\beta}(k) \\ . \\ . \\ . \\ i_{\alpha\beta}(k-N) \end{bmatrix} \tag{23}$$

where A is the matrix of measured line currents and the difference between the inverter and grid voltages over N samples, x is the vector of unknown β_1 and β_2 (estimated), and b is the vector of the measured currents. From (23), an online impedance estimation model, as portrayed in Figure 8, can be devised using RLS algorithm.

If $u_{\alpha\beta}$ is the computed difference between the inverter and grid voltage and b is a vector of measured values of the axis current, then β_1 and β_2 can be estimated in a window of N samples. Note that from equation (21),

$$L_g = \frac{T_s}{\beta_2} \; and \; R_g = \frac{1 - \beta_1}{\beta_2} \tag{24}$$

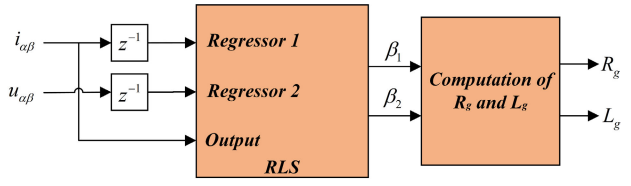

FIGURE 8. Estimation model for grid resistance and inductance.

Therefore, a change in the values of the impedance will result in the update of β_1 and β_2 allowing estimation in variations of the inductances and resistances at PCC. For the estimation of grid parameters, either the α or β components of the grid currents and voltages can be utilized. Furthermore, the scheme presented in Figure 9 is suggested to improve the reference tracking accuracy of the grid-connected system and simultaneously be resilient to possible fluctuations of grid parameters.

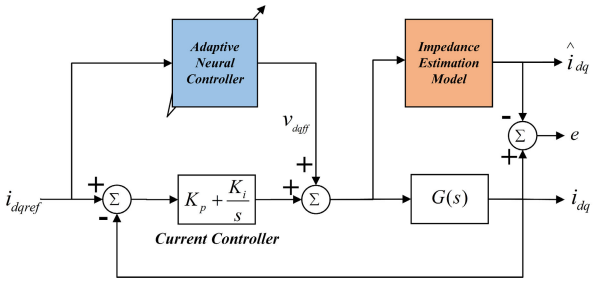

FIGURE 9. General control structure of neural network-based adaptive current controller.

This is made possible by adding a feedforward voltage to the output of the PI controller in the synchronous rotating reference frame. The simple feedforward linear neural network can be formulated to construct the inverse of the system with β_1 and β_2 as the weights of the ADALINE. From equation (22), it can be deduced that the inverse of the system can be expressed as

$$u_{\alpha\beta}(k-1) = \frac{1}{\beta_2} i_{\alpha\beta}(k) - \frac{\beta_1}{\beta_2} i_{\alpha\beta}(k-1) \tag{25}$$

The system inverse is independent of the reference frame it is implemented in. As such, by integrating the neural network with the PI controller, equation (25) is transformed onto the synchronous rotating reference frame as

$$u_{dq}(k-1) = \frac{1}{\beta_2} i_{dq}(k) - \frac{\beta_1}{\beta_2} i_{dq}(k-1) \tag{26}$$

As equation (26), shows, there are no poles allowing the system to be stable. Substituting the grid currents for the corresponding direct and quadrature reference and measured values ($i_{dqref}(k)$ and $i_{gdq}(k-1)$) creates the feedforward neural controller. Adding the inverse of the plant to the control signal should improve the grid side inverter's transient behavior, settling time and be resilient to stochastic changes in grid impedance as the weights are determined online. Subsequently, denoting the output of the ADALINE neural network as v_{dqff}, the final equation for the neural controller is given as

$$v_{dqff} = \frac{1}{\beta_2} i_{dqref}(k) - \frac{\beta_1}{\beta_2} i_{gdq}(k-1) \tag{27}$$

Intrinsically, the decoupled control with PI regulators can be utilized to enhance the stability of the grid-connected VSI and the closed-loop inverter currents by adding the output of the adaptive controller with the cross-coupling for generation

of the reference direct and quadrature axis voltages (v_{dref} and v_{qref}) as expressed in equation (28). The introduced feedforward terms (v_{dff} and v_{qff}) are the output of the feedforward neural controller used to enhance the control of the direct and quadrature currents and they eventually improve the injection of the active and reactive power components of the inverter independently.

$$\begin{aligned} v_{dref} &= \left(K_p + \frac{K_i}{s}\right)\left(i_{dref} - i_{gd}\right) + \omega L i_{gq} + v_{gd} + v_{dff} \\ v_{qref} &= \left(K_p + \frac{K_i}{s}\right)\left(i_{qref} - i_{gq}\right) - \omega L i_{gd} + v_{gq} + v_{qff} \end{aligned} \tag{28}$$

The control parameters for the grid side inverter are stated in Table 4.

TABLE 4. Adaptive VOC parameters.

	K_p	K_i
DC Link Controller	0.7	15
Direct Axis Current Controller	4	350
Quadrature Axis Current Controller	4	350
Double SOGI PLL	150	5000
Controller Sample Time (T_s)	100µs	
Covariance Matrix	[5x10^{-3} 5x10^{-3}]	
Forgetting Factor	0.99	

C. RECURSIVE LEAST SQUARES ESTIMATOR

Recursive Least Squares (RLS) estimator finds the coefficients that minimize a weighted linear cost function related to a set of deterministic input signals. For a linear system that can be stated as $Ax \approx b$, and given as a vector of estimated parameters with $L(k)$ as the update gain, the standard recursive form can be described as

$$x(k) = x(k-1) + L(k)[b(k) - A^T(k)x(k-1)] \tag{29}$$

The Forgetting Factor (λ), practically between 0 and 1, strongly influences the estimation of parameters by the RLS. It acts as a weight that exponentially reduces for more remote. A small λ makes the algorithm more sensitive to parameter changes and noise, while a very high value may be insensitive to rapidly changing parameters [25]. The concept of forgetting is more effective for systems where parameters vary continuously but slowly, such as grid impedance. This gives recently observed data more emphasis while estimating parameters in real time. This leads to the following expression for the covariance matrix.

$$P(k) = [1 - L(k)A^T(k)]P(k-1)\frac{1}{\lambda} \tag{30}$$

The covariance matrix is divided by the forgetting factor ($\lambda < 1$) at each successive update which decelerates the vanishing of the matrix [25]. Therefore, a reasonable value of $\lambda = 1$ and $\lambda = 0.99$ with a covariance matrix of $[1 \times 10^{-4}\ 1 \times 10^{-4}]$ and $[5 \times 10^{-3}\ 5 \times 10^{-3}]$ can be chosen to allow estimation of the inertia/friction coefficient of the induction generator and varying grid impedance respectively. The chosen forgetting factor and covariance matrix values should also concurrently be resilient to noise in the system originating from switching of the inverter, oscillations in speed and torque or distortions in the grid voltage at high impedance [26]. For this research, a sampling frequency of 10kHz produced the best estimation accuracy with an error of less than 5% under the rated operating conditions of the induction generator. The overall proposed adaptive control scheme for back-to-back connected inverters in WECS is shown in Figure 10.

V. SIMULATION RESULTS

The designed control technique is implemented on a grid-interfaced wind turbine generator emulated using the parameters of a 2.2kW induction motor connected to a 415V/50Hz grid. All the modelling and control parameters are specified in Tables 1-4. To validate the performance of the proposed adaptive controllers, the PI+AFN neural controllers for both the AFOC and AVOC were tested under nominal operating conditions, sudden wind speed variation and changing grid impedance at PCC.

A. NOMINAL OPERATING CONDITIONS

In the first case the grid impedance is kept constant with an inductance of 1mH and a resistance of 0.15Ω. The Double Second Order Generalized Integrator (DSOGI) Phase Locked Loop (PLL) is utilized to synchronize the grid-side inverter with the electricity network as it has superior performance. At t=0s the turbine is given a reference speed of 157rads/s. At this point in time, power is drawn from the grid to start the WEC generator. At t=0.5s the turbine is subjected to constant wind speed of 3.9 m/s which translates to about -14 Nm of load torque subjected to the generator shaft. Figure 11 and Figure 12 show the estimated mechanical inertia and friction coefficient of the induction generator while Figure 13 and Figure 14 portray the estimated grid inductance and resistance respectively under normal operating condition. Using the information of the estimated parameters of the machine, the weights of the AFN controller (α_1 and α_2) is created for the speed PI controller. Similarly, the value of the grid impedance is utilized to produce the weights of the AFN controller (β_1 and β_2) for the direct and quadrature PI current controllers.

Analyzing the generator's speed response (Figure 15) in the transient region, it can be noted that PI+AFN has a faster dynamical response with lower overshoots and reduced settling time.

Due to the enhanced speed response with the PI+AFN, the electromagnetic torque response of the turbine machine is also faster at the transient stage, as shown in Figure 16. It can be visualized that the proposed AFN technique eliminates the overshoot of the torque when the machine starts and when a constant wind speed is applied to produce a torque at the shaft at t=0.5s.

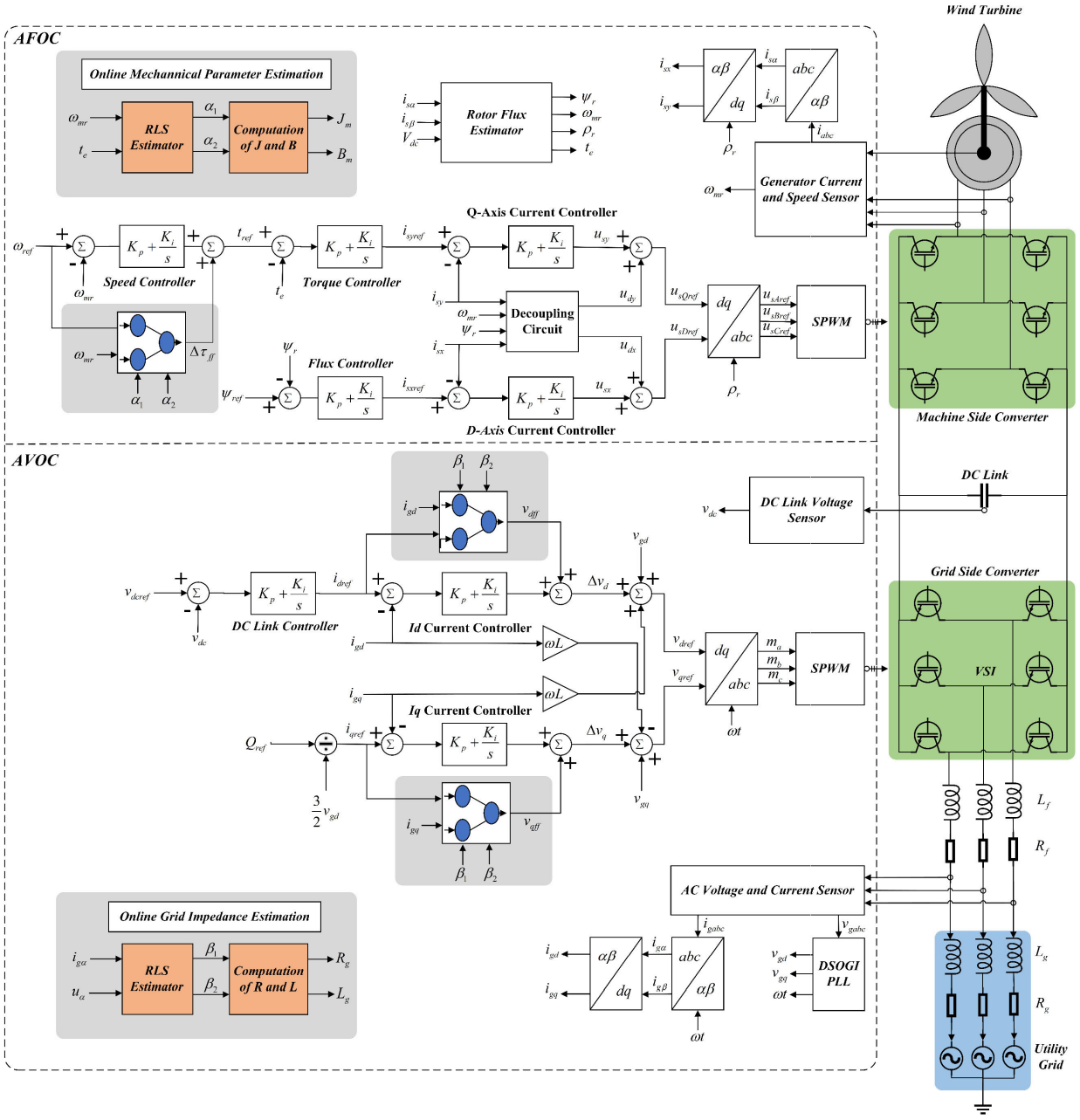

FIGURE 10. Proposed AFOC and AVOC control scheme for WECS.

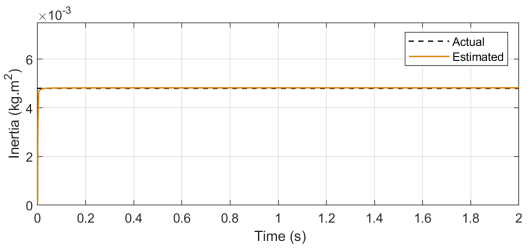

FIGURE 11. Estimation model for grid resistance and inductance.

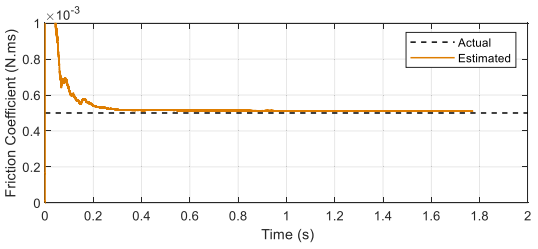

FIGURE 12. Estimation of generator friction coefficient.

The inclusion of the proposed adaptive technique for the grid side converter controlled using VOC improves the response of the injected direct and quadrature currents leading to more robust control of active and reactive power control at PCC, as shown in Figure 17 and Figure 18. Initially, power is drawn from the grid to start the turbine, and then

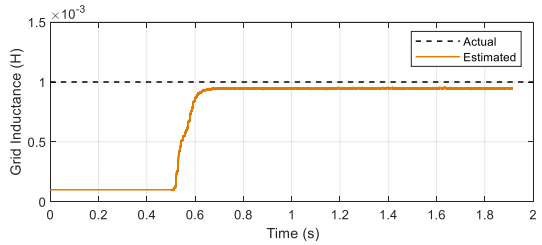

FIGURE 13. Estimation of grid inductance.

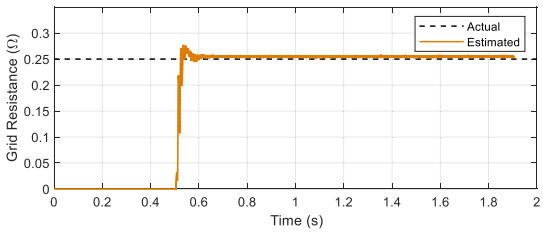

FIGURE 14. Estimation of grid resistance.

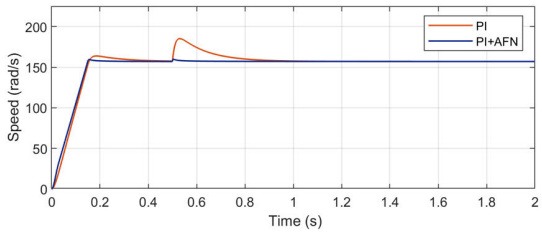

FIGURE 15. Turbine shaft speed.

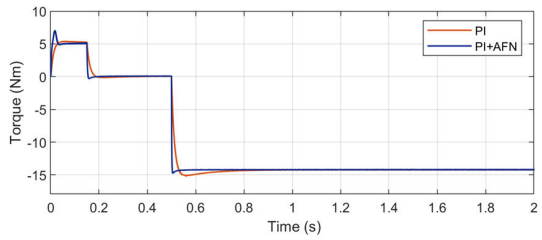

FIGURE 16. Electromagnetic torque of the machine.

at t=0.5, the turbine is subjected to a wind speed of 3.9 m/s translating to -14 Nm of negative torque on the shaft. Negative torque makes the rotor speed higher than the synchronous speed, thus enabling approximately 1.75kW of active power to be injected from the machine to the grid, which can be visualized after 0.5s.

Notably, PI+AFN has a better response regarding overshoot minimization and faster settling time of the active and reactive powers at the PCC. Additionally, to ensure the optimum power factor, the quadrature axis of the VOC is given a reference of zero. PI+AFN exhibits superior reference tracking ability and maintains the reactive power to zero with minimum fluctuations.

B. WIND SPEED VARIATION

The wind has a stochastically varying nature, i.e., it never has a constant value or profile because wind speed at any location

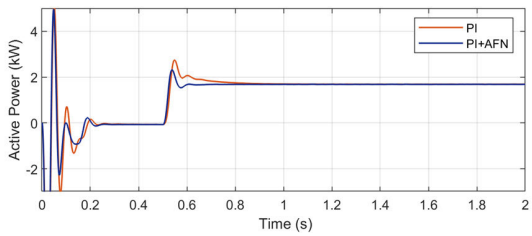

FIGURE 17. Active power at PCC.

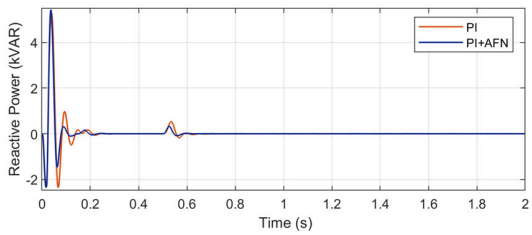

FIGURE 18. Reactive power at PCC.

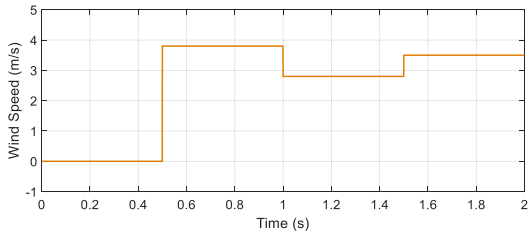

FIGURE 19. Wind speed profile.

on earth changes abruptly throughout the day. This can have consequences for the power delivery of WECS if appropriate adaptive actions are not taken. For simulation purposes, the system is subjected to a varying wind speed profile as shown in Fig. 19. A 3.8m/s step wind speed is given at 0.5s, followed by 3.5m/s at 1s and 2.8m/s at 1.5s. At the instance of these variations, the speed of the generator encounters high overshoots and disturbances when the classical speed PI controller is used in the FOC structure. However, when the proposed PI+AFN controller is used, these overshoots are eliminated as seen Fig. 20. As a result of the smooth transition and faster transient during wind speed variation, the torque response also has a faster and more robust behavior as seen in Fig. 21. The direct translation of wind speed to electromagnetic torque portrays that the PI+AFN controller has a faster and smoother response when compared to the classical PI controller.

One of the key objectives of using the enhanced technique on the grid side converter is to improve the quality of power delivered to the grid under dynamically changing power reference. At varying wind speeds, varied torque is applied to the turbine shaft, which has a linear correlation with the power injected into the grid. In this case, for wind speeds of 3.8 m/s, 2.8 m/s and 3.5 m/s, a total of 1.75kW, 1kW and 1.5kW of power is injected into the grid. As seen in Figure 22, the active power injection to the grid is improved by using

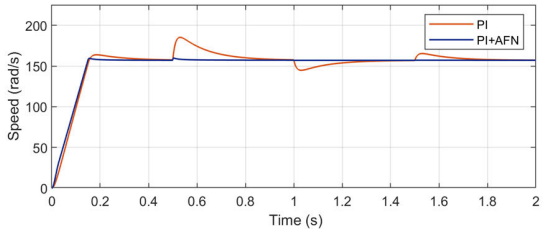

FIGURE 20. Wind turbine speed.

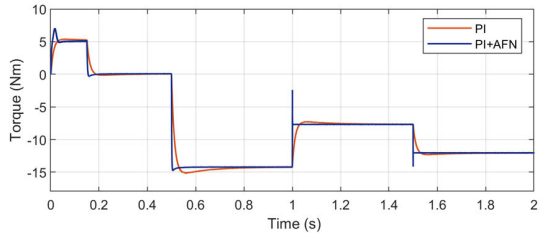

FIGURE 21. Variation in the electromagnetic torque on the machine.

the PI+AFN, allowing a better transition from one operating point to another with a faster settling time.

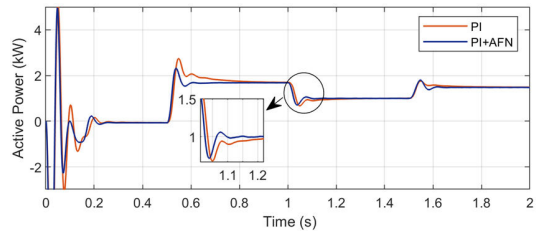

FIGURE 22. Changes in active power at PCC.

The reactive power at PCC undergoes fluctuations when the wind speed changes. As seen in Figure 23, the PI+AFN controller has superior performance in minimizing oscillations in the reactive power.

An important factor that affects power quality at PCC is the presence of current harmonics. The Total Harmonic Distortion (THD) is the sum of all the harmonic components of the sinusoidal waveform compared to the fundamental component [27]. High harmonics cause power losses, increased flow of eddy currents, overheating of power electronic equipment, stress on the inverter, and tripping of circuit breakers. According to the IEEE Standard 519-2014 (Recommended Practice and Requirements for Harmonic Control in Electric Power Systems), the current total harmonic distortion at PCC for 120V to 69kV systems should be below 5% [28]. The three-phase currents at PCC have been analyzed for harmonic content, and the results are stated in Table 5 at different wind speeds or power levels.

THD increases with decreasing power injection or at low wind speeds. The PI+AFN controller can reduce current harmonics under all conditions of wind speed variation much better than the PI controller.

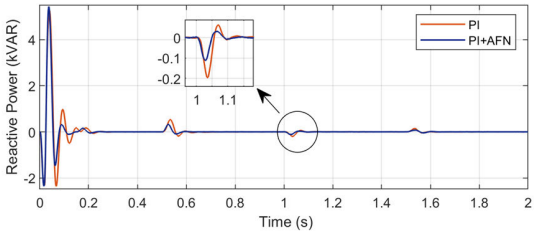

FIGURE 23. Reactive power at PCC.

TABLE 5. Current THD analysis at different wind speeds.

	3.8m/s	3.5m/s	2.8m/s
PI	2.17%	2.66%	4.28%
PI+AFN	1.87%	2.01%	3.39%

C. GRID IMPEDANCE VARIATION

Considering the system as a weak grid, the impedance is subjected to vary when there are abrupt loading conditions or penetration of RES into the network. Therefore, in this case, a test has been performed to understand the viability of the proposed technique under the influence of varying grid impedance. Figure 24 and Figure 25 show the speed and torque of the machine, which is subjected to a nominal wind speed of 3.8 m/s at t= 0.5s for a maximum torque of -14Nm.

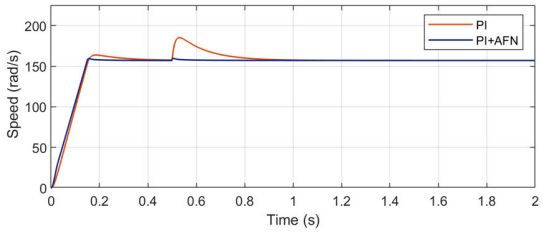

FIGURE 24. Wind turbine speed.

It is noteworthy that the speed and electromagnetic toque of the turbine is not affected by the variation of the grid impedance because of the independent decoupled nature of the FOC from the VOC. The grid inductance is varied at t=0.5s, 1s and 1.5s to 1mH, 8mH and 4mH respectively as seen in Figure 26. Figure 27 shows the active power of 1.75kW injected into the grid. PI+AFN is effective in minimizing fluctuations and oscillation in the active and reactive power when the system is subjected to change in grid impedance compared to the conventional PI controller.

D. INTEGRAL TIME ERROR

To justly validate the performance of any controller, it is essential to compute the Integral Squared Error (ISE) or the Integral Time Absolute Error (ITAE). ISE is the squared of the error over time, whereas ITAE multiplies the absolute error with time, allowing it to weigh errors more heavily in a system after a long time than those existing at the beginning. A low error-index is desired in control systems applications.

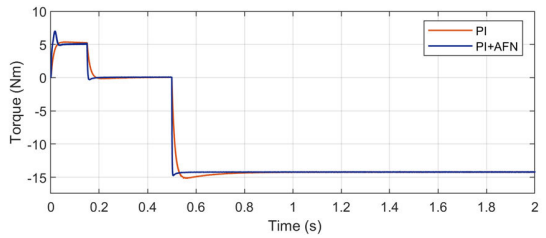

FIGURE 25. Electromagnetic torque on the machine.

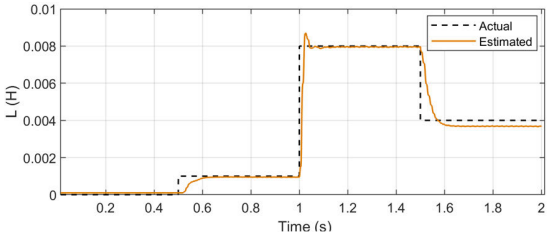

FIGURE 26. Estimation of varying grid inductance.

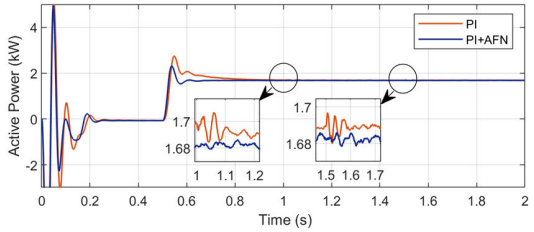

FIGURE 27. Active power during grid impedance variation

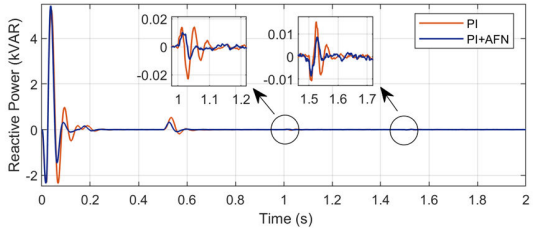

FIGURE 28. Reactive power during grid impedance variation.

The errors have been evaluated using equations (31) - (33).

$$ISE = \int_0^\infty e^2(t)dt \tag{31}$$

$$IAE = \int_0^\infty |e(t)|dt \tag{32}$$

$$ITAE = \int_0^\infty t|e^2(t)|dt \tag{33}$$

Table 6 summarizes the performance index of the speed PI and PI+AFN controller in the FOC at various wind speeds while Table 7 shows the performance index of the current PI controllers and the PI+AFN controller in the VOC with varying grid impedance. In both cases, the error-index is maintained at a minimum with the developed adaptive control strategy, thus improving the performance of the speed and current controllers under various dynamical conditions.

TABLE 6. Speed controller performance index at different wind speeds.

	3.8m/s		3.5m/s		2.8m/s	
	PI	PI+AFN	PI	PI+AFN	PI	PI+AFN
ISE	82.65	0.05	102.3	0.6	96.13	0.06
IAE	6.15	0.06	9.26	0.24	8.02	0.09
ITAE	2.87	0.02	6.97	0.29	4.94	0.05

TABLE 7. Current controller performance index at different grid impedance.

	L_g = 1mH		L_g = 4mH		L_g = 8mH	
	PI	PI+AFN	PI	PI+AFN	PI	PI+AFN
ISE	2.77	2.65	2.78	2.69	2.78	2.67
IAE	0.49	0.32	0.55	0.44	0.52	0.41
ITAE	0.05	0.02	0.13	0.09	0.08	0.05

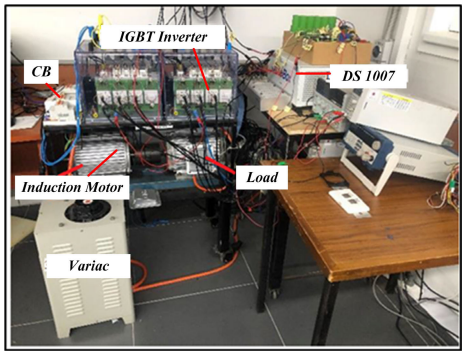

FIGURE 29. Experimental test rig.

VI. EXPERIMENTAL VALIDATION

For testing the proposed adaptive control technique in hardware, a wind turbine emulator was developed using a 2.2kW induction motor coupled to another motor commanded in torque. A picture of the test rig is provided in Figure 29.

The overall schematic is shown in Figure 30. Other components in the circuit include:

- Semikron IGBT 20kVA inverter.
- 10A NHP MOD6 circuit breakers for protection.
- 5V BNC cables for carrying the PWM signals.
- Incremental speed encoder (DFS60B-S4PK1000) mounted on the rotor shaft.
- Driver circuit comprising of the open collector (LS7406) and hex inverter trigger (LS7414) chips.

The control platform DSPACE Auto Box 1007 generates control signals for the machine and acquires data via its analogue input channels. Inverter pulses are produced at the digital I/O pins at 10kHz.

To show the performance of the adaptive control technique, the generator was first operated at nominal conditions. An estimation of the inertia and friction coefficient as acquired using the speed and electrical torque of the machine

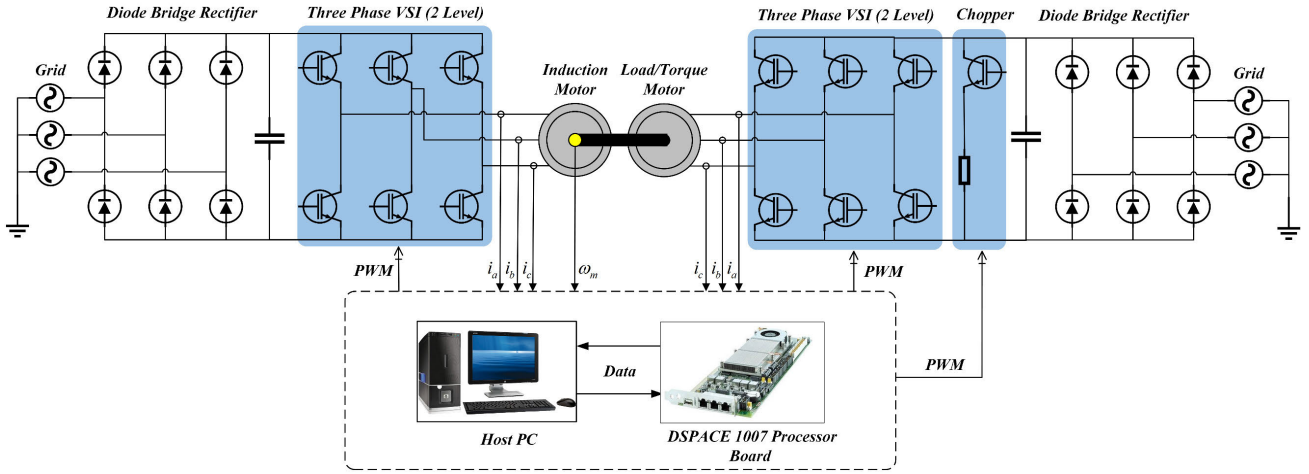

FIGURE 30. Wind turbine emulator schematic.

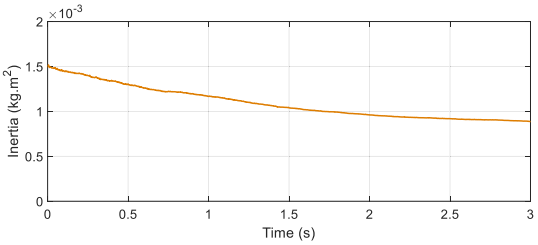

FIGURE 31. Estimated generator inertia.

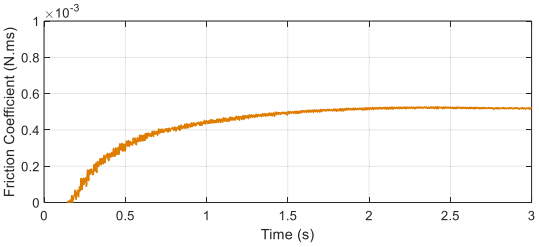

FIGURE 32. Estimated generator friction coefficient.

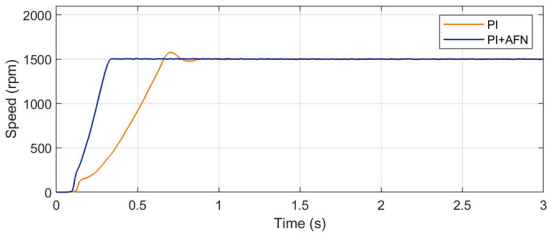

FIGURE 33. Speed response under nominal operation.

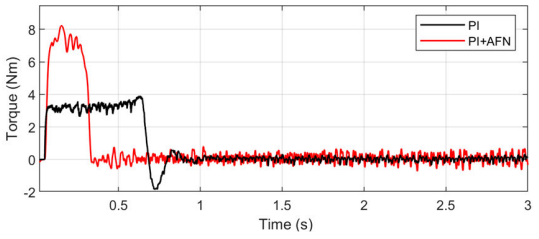

FIGURE 34. Machine torque under nominal operating.

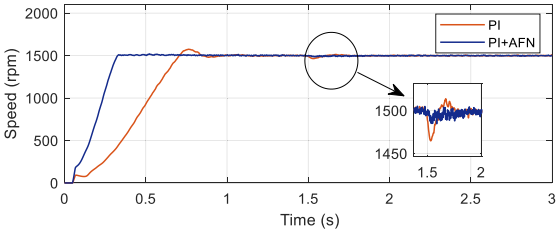

FIGURE 35. Generator speed response with applied torque.

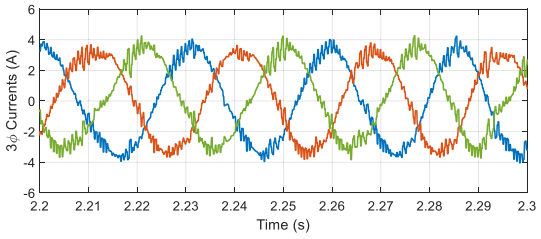

FIGURE 36. Three-phase machine currents.

is portrayed in Figure 31 and Figure 32, respectively. The estimation convergence highly depends on the values of the forgetting factor and covariance matrix of the RLS. As such, these parameters must be appropriately tuned to give reasonable accuracy with fast convergence.

As for the speed response (Figure 33), using the feedforward controller proved to significantly improve the transient stage of the generator speed with faster settling time and reduced overshoots. With the PI controller, the speed reaches steady state at approximately 1s; however, with the PI+AFN controller, the time is reduced to 0.34s. The torque response (Figure 34) also experiences a similar trend. Although a

high overshoot is seen initially with the PI+AFN controller, a steady state is reached in a shorter time to ensure the machine's stability than the PI controller, which displays slower dynamics.

In the second test case, a step torque of 5Nm is applied on the machine shaft at 1.5s. As expected, the feedforward approach is better at handling sudden variations in operating conditions, as shown in Figure 35. This demonstrates the ability of the controller to maintain the generator speed during variations in wind speed. The three-phase currents produced at the machine terminal are shown in Figure 36.

VII. CONCLUSION

This paper outlined adaptive control strategies for improving the power delivery of grid-connected wind turbine induction generators during abrupt changes in wind speed and grid impedance variation. Adaptive feedforward linear neural network controllers are proposed in the synchronous reference frame, which is constructed via the real-time estimation of mechanical parameters of the induction generator and grid impedance using the RLS algorithm.

The PI+AFN controller is superior in controlling the power injection into the grid under the rapidly changing power output of the wind generator and fluctuations in grid impedance. Not only does the adaptive strategy reduce the settling time and overshoots of the speed response but also decrease the THD of the current injected at PCC. Due to the enhanced stability of the back-to-back inverters, the overall dynamics of the injected active and reactive powers at PCC are significantly improved. It is also noted that the integral-time errors of the speed and current PI controllers in the AFOC and AVOC are much lower than when only the PI controller is used, thus guaranteeing superior reference tracking. The control scheme has also been verified in hardware using a 2.2kW induction motor to emulate the wind generator. Notably, the proposed control architecture does not have high computational requirements and can be implemented with FPGA or DSP boards.

The proposed control approach will likely be further improved for future works by incorporating discretization time delays in the estimation and feedforward neural network model. This is expected to increase the estimation accuracy and further enhance system performance. The scheme can also be applied to other distributed generation units and microgrids to maintain stability and resilience under weak grid conditions. This will allow greater penetration of renewable energy into the electricity network while preserving power quality under high-impedance electricity networks.

REFERENCES

[1] S. M. Tripathi, A. N. Tiwari, and D. Singh, "Grid-integrated permanent magnet synchronous generator based wind energy conversion systems: A technology review," *Renew. Sustain. Energy Rev.*, vol. 51, pp. 1288–1305, Nov. 2015, doi: 10.1016/J.RSER.2015.06.060.

[2] M. A. Mostafa, A. El-Hay, and M. M. Elkholy, "Recent trends in wind energy conversion system with grid integration based on soft computing methods: Comprehensive review, comparisons and insights," *Arch. Comput. Methods Eng.*, vol. 2022, vol. 1, pp. 1–40, Nov. 2022, doi: 10.1007/S11831-022-09842-4.

[3] B. Jain, S. Jain, and R. K. Nema, "Control strategies of grid interfaced wind energy conversion system: An overview," *Renew. Sustain. Energy Rev.*, vol. 47, pp. 983–996, Jul. 2015, doi: 10.1016/J.RSER.2015.03.063.

[4] M. Ali, S. M. Amrr, and M. Khalid, "Speed control of a wind turbine-driven doubly fed induction generator using sliding mode technique with practical finite-time stability," *Frontiers Energy Res.*, vol. 10, p. 1326, Sep. 2022, doi: 10.3389/FENRG.2022.970755.

[5] K. Senthilnathan and K. Iyswarya Annapoorani, "A review on back-to-back converters in permanent magnet synchronous generator based wind energy conversion system," *Indones. J. Electr. Eng. Comput. Sci.*, vol. 2, no. 3, pp. 583–591, Jun. 2016, doi: 10.11591/IJEECS.V2.I3.PP583-591.

[6] H. Wu and J. Huang, "Control of induction motor drive based on ADRC and inertia estimation," in *Proc. IEEE Int. Electr. Mach. Drives Conf. (IEMDC)*, May 2019, pp. 1607–1612, doi: 10.1109/IEMDC.2019.8785393.

[7] H. Guolian, H. Liping, and Z. Jianhua, "Variable universe adaptive fuzzy PI control used in VSCF wind power generator system," in *Proc. 8th World Congr. Intell. Control Autom.*, Jul. 2010, pp. 4870–4874, doi: 10.1109/WCICA.2010.5554892.

[8] Q. Duan, F. Hao, and S. Feng, "Adaptive fuzzy control used in DFIG VSCF wind power generator system," in *Proc. 7th World Congr. Intell. Control Autom.*, 2008, pp. 29–32, doi: 10.1109/WCICA.2008.4592898.

[9] Y. Saidi, "Adaptive control of wind turbine generators for power capture optimization by using integral backstepping approach during partial-load operation," *J. Control. Autom. Electr. Syst.*, vol. 32, no. 4, pp. 1041–1052, Aug. 2021, doi: 10.1007/S40313-021-00716-x.

[10] C. Eddahmani, H. Mahmoudi, M. E. Azzaoui, and K. Boudaraia, "Backstepping and adaptive control for variable wind speed turbine based on PM synchronous generator," in *Proc. 14th Int. Multi-Conf. Syst., Signals Devices (SSD)*, Mar. 2017, pp. 785–789, doi: 10.1109/SSD.2017.8167020.

[11] S.-J. Hong, H.-W. Kim, and S.-K. Sul, "A novel inertia identification method for speed control of electric machine," in *Proc. IEEE IECON. 22nd Int. Conf. Ind. Electron., Control, Instrum.*, Aug. 1996, pp. 1234–1239, doi: 10.1109/IECON.1996.566056.

[12] M. A. Soliman, H. M. Hasanien, A. Al-Durra, and I. Alsaidan, "A novel adaptive control method for performance enhancement of grid-connected variable-speed wind generators," *IEEE Access*, vol. 8, pp. 82617–82629, 2020, doi: 10.1109/ACCESS.2020.2991689.

[13] A. Timbus, M. Liserre, R. Teodorescu, P. Rodriguez, and F. Blaabjerg, "Evaluation of current controllers for distributed power generation systems," *IEEE Trans. Power Electron.*, vol. 24, no. 3, pp. 654–664, Mar. 2009, doi: 10.1109/TPEL.2009.2012527.

[14] I. S. Mohamed, S. Rovetta, T. D. Do, T. Dragicevic, and A. A. Z. Diab, "A neural-network-based model predictive control of three-phase inverter with an output *LC* filter," *IEEE Access*, vol. 7, pp. 124737–124749, 2019, doi: 10.1109/ACCESS.2019.2938220.

[15] J. De Kooning, J. Van De Vyver, J. D. M. De Kooning, T. L. Vandoorn, and L. Vandevelde, "Grid voltage control with wind turbine inverters by using grid impedance estimation," in *Proc. IET Conf. Publications*, 2014, Art. no. CP651, doi: 10.1049/cp.2014.0846.

[16] M. Céspedes and J. Sun, "Online grid impedance identification for adaptive control of grid-connected inverters," in *Proc. IEEE Energy Convers. Congr. Expo. (ECCE)*, Sep. 2012, pp. 914–921, doi: 10.1109/ECCE.2012.6342721.

[17] J. Kukkola, M. Routimo, and M. Hinkkanen, "Real-time grid impedance estimation using a converter," in *Proc. IEEE Energy Convers. Congr. Expo. (ECCE)*, Sep. 2019, pp. 6005–6012, doi: 10.1109/ECCE.2019.8912681.

[18] X. Fu and S. Li, "Control of single-phase grid-connected converters with LCL filters using recurrent neural network and conventional control methods," *IEEE Trans. Power Electron.*, vol. 31, no. 7, pp. 5354–5364, Jul. 2016, doi: 10.1109/TPEL.2015.2490200.

[19] X. Fu and S. Li, "A novel neural network vector control for single-phase grid-connected converters with L, LC and LCL filters," *Energies*, vol. 9, no. 5, p. 328, Apr. 2016, doi: 10.3390/EN9050328.

[20] M. Cirrincione, M. Pucci, and G. Vitale, "Growing neural gas (GNG) based maximum power point tracking for high performance VOC-FOC based wind generator system with an induction machine," in *Proc. IEEE Energy Convers. Congr. Expo.*, Sep. 2009, pp. 1603–1610, doi: 10.1109/ECCE.2009.5316549.

[21] M. Cirrincione, M. Pucci, and G. Vitale, "Neural MPPT of variable pitch wind generators with induction machines in a wide wind speed range," in *Proc. IEEE Energy Convers. Congr. Expo.*, Sep. 2011, pp. 857–864, doi: 10.1109/ECCE.2011.6063860.
[22] R. Prasad, D. Kumar, S. Chand, A. Fagiolini, H. Mudaliar, M. D. Benedetto, and M. Cirrincione, "Enhancing speed loop PI controllers with adaptive feed-forward neural networks: Application to induction motor drives," in *Proc. 25th Int. Conf. Electr. Mach. Syst. (ICEMS)*, Nov. 2022, pp. 1–6, doi: 10.1109/ICEMS56177.2022.9983335.
[23] M. Cirrincione, M. Pucci, and V. Gianpaolo, "Control techniques of induction machines drives," in *Power Converters and AC Electrical Drives with Linear Neural Networks*. Boca Raton, FL, USA: CRC Press, Dec. 2017, pp. 189–260, doi: 10.1201/B12073-5.
[24] S. S. Chand, R. Prasad, H. Mudaliar, D. Kumar, A. Fagiolini, M. Di Benedetto, and M. Cirrincione, "Enhanced current loop PI controllers with adaptive feed-forward neural network via estimation of grid impedance: Application to three-phase grid-tied PV inverters," in *Proc. IEEE Energy Convers. Congr. Expo. (ECCE)*, Oct. 2022, pp. 1–8, doi: 10.1109/ECCE50734.2022.9947752.
[25] A. Vahidi, A. Stefanopoulou, and H. Peng, "Recursive least squares with forgetting for online estimation of vehicle mass and road grade: Theory and experiments," *Vehicle Syst. Dyn.*, vol. 43, no. 1, pp. 31–55, Jan. 2005, doi: 10.1080/00423110412331290446.
[26] H. K. Mudaliar, A. Fagiolini, M. Cirrincione, S. S. Chand, R. Prasad, and D. Kumar, "Adaptive feed-forward neural network for wind power delivery," in *Proc. 25th Int. Conf. Electr. Mach. Syst. (ICEMS)*, Nov. 2022, pp. 1–5, doi: 10.1109/ICEMS56177.2022.9983098.
[27] N. Malla, U. Tamrakar, D. Shrestha, Z. Ni, and R. Tonkoski, "Online learning control for harmonics reduction based on current controlled voltage source power inverters," *IEEE/CAA J. Autom. Sinica*, vol. 4, no. 3, pp. 447–457, Jul. 2017, doi: 10.1109/JAS.2017.7510541.
[28] *IEEE Recommended Practice and Requirements for Harmonic Control*, Standard 519TM-2014 ANSI/IEEE Std. 519, 2014, pp. 5–9, Accessed: Jun. 15, 2023. [Online]. Available: https://ieeexplore.ieee.org/document/6826459

SHYAMAL SHIVNEEL CHAND (Student Member, IEEE) received the B.E. degree in electrical and electronics and the M.Sc. degree in engineering from The University of the South Pacific (USP), Fiji, in 2020 and 2022, respectively. He is currently a full-time Teaching Assistant with USP. His current research interests include inverter modeling and control with emphasis on developing resilient connection with the grid, integration of renewable energy systems (photovoltaic and wind) into microgrids, and the advanced control of electrical machines (induction motor, synchronous reluctance motor, and permanent magnet synchronous motor). He was a recipient of the National Toppers Scholarship (NTS) and the Pacific Scholarship for Excellence in Research and Innovation (PSERI) for his undergraduate and graduate studies.

RAVNEEL PRASAD received the B.Eng. degree in electrical and electronics and the M.Sc. degree in engineering from The University of the South Pacific, Fiji, in 2020 and 2022, respectively. Currently, he is a Teaching Assistant with the School of Information Technology, Engineering, Mathematics and Physics (STEMP), The University of the South Pacific. His current research interests include electrical drives, power electronics, neural networks, renewable energy, wind energy conversion systems, and grid-connected solar systems. He was a recipient of the Nation Toppers Scheme and the Pacific Scholarship for Excellence in Research and Innovation (PSERI) scholarships for the tertiary education degree program.

HIYE K. MUDALIAR received the B.E. degree in electrical and electronics engineering and the M.Sc. degree in engineering from The University of the South Pacific, Suva, Fiji, in 2017 and 2019, respectively. He is currently pursuing the Ph.D. degree in electrical engineering with the University of Palermo, Sicilia, Italy. From 2017 to 2018, he was a Research Assistant with The University of the South Pacific. His current research interests include power electronics, control and modeling, renewable energy systems, and electrical machines and drives.

DHIRENDRAN MUNITH KUMAR (Graduate Student Member, IEEE) received the B.E. degree in electrical and electronics engineering and the M.Sc. degree in engineering from The University of the South Pacific, Suva, Fiji, in 2017 and 2019, respectively. He is currently pursuing the Ph.D. degree in engineering with the University of Palermo, Italy. From 2017 to 2022, he was a Teaching Assistant with The University of the South Pacific. His current research interests include power electronics, control and modeling of reversible heat pumps, and motor drives.

ADRIANO FAGIOLINI (Member, IEEE) received the M.S. degree in computer science engineering and the Ph.D. degree in robotics and automation from the University of Pisa, in 2004 and 2009, respectively. He enrolled in the Summer Student Program with the European Center for Nuclear Research (CERN), Geneva, in 2002. He was a Visiting Researcher with the Department of Mechanical Engineering, University of California at Riverside, in 2015 and 2017, and the Department of Energy, IUT Longwy Universiteì de Lorraine, France, in 2019. He is currently an Assistant Professor with the University of Palermo, Italy. In 2008, he led the Team of the University of Pisa, during the first European Space Agency's Lunar Robotics Challenge, which resulted in a second-place prize for the team. He was one of the recipients of the IEEE ICRA Best Manipulation Paper Award, in 2005.

MARCO DI BENEDETTO (Member, IEEE) received the M.Eng. degree in electronic engineering from the University of Roma Tor Vergata, Rome, Italy, in 2014, and the Ph.D. degree in mechanical and industrial engineering from Roma Tre University, Rome, in 2018. Since November 2018, he has been a Research Fellow with the Center of Power Electronics and Drives (C-PED), Roma Ter University. His current research interest includes hardware and FPGA control design for multilevel power converter topologies.

MAURIZIO CIRRINCIONE (Senior Member, IEEE) received the Laurea degree in electrical engineering from the Polytechnic University of Turin, Turin, Italy, in 1991, and the Ph.D. degree in electrical engineering from the University of Palermo, Palermo, Italy, in1996. Since September 2005, he has been a Professor with Université de Technologie de Belfort-Montbéliard, Belfort, France. Since April 2014, he has been the Head of the School of Engineering and Physics, The University of the South Pacific, Suva, Fiji. His current research interests include neural networks for modeling and control, system identification, intelligent control, power electronics, renewable energy systems, and electrical machines and drives. He was a recipient of the 1997 E. R. Caianiello Prize for the Best Italian Ph.D. thesis on neural networks.

Open Access funding provided by 'Università degli Studi di Palermo' within the CRUI CARE Agreement